Chemical Engineering Journal 368 (2019) 235–243

Contents lists available at ScienceDirect

Chemical Engineering Journal

journal homepage: www.elsevier.com/locate/cej

Superior potassium-ion hybrid capacitor based on novel P3-type layered $K_{0.45}Mn_{0.5}Co_{0.5}O_2$ as high capacity cathode

Hari Vignesh Ramasamy[a], Baskar Senthilkumar[b,*], Prabeer Barpanda[b], Yun-Sung Lee[a,*]

[a] Faculty of Applied Chemical Engineering, Chonnam National University, Gwangju 61186, Republic of Korea
[b] Faraday Materials Laboratory (FaMaL), Materials Research Centre, Indian Institute of Science (IISc), C.V. Raman Avenue, Bangalore 560012, India

HIGHLIGHTS

- A novel P3-type layered $K_{0.45}Mn_{0.5}Co_{0.5}O_2$ has been synthesized using conventional sol-gel method.
- It exhibits excellent cyclic stability with 80% capacity retention up to 50 cycles.
- When coupled with commercial AC, the KIC could provide a very high energy and power density of 43 Wh kg^{-1} and 30 kW kg^{-1}.
- The KIC retains 88% of its energy density with an ultrahigh stability of up to 30,000 cycles at 10 A g^{-1}.

GRAPHICAL ABSTRACT

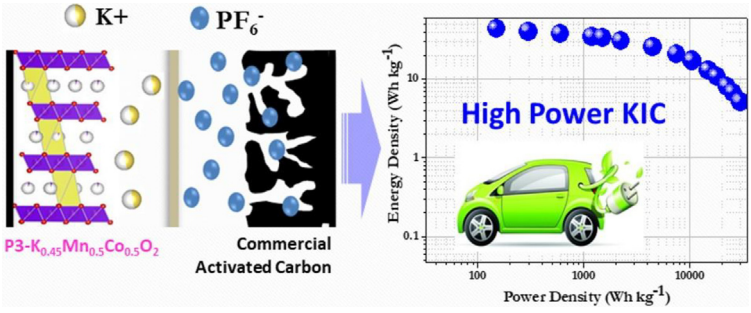

ARTICLE INFO

Keywords:
Potassium-ion capacitor
P3-$K_{0.45}Mn_{0.5}Co_{0.5}O_2$
Energy density
Potassium-ion intercalation
Capacity

ABSTRACT

Herein, we demonstrate a new non-aqueous potassium-ion hybrid capacitor (KIC) using novel P3-$K_{0.45}Mn_{0.5}Co_{0.5}O_2$ and commercial activated carbon (CAC) as the cathode and anode, respectively. A simple sol–gel method is used to synthesize the P3-$K_{0.45}Mn_{0.5}Co_{0.5}O_2$ cathode nanoplatelets. The structural and morphological studies are performed using various characterization techniques, and their electrochemical performances are studied in half-cell configurations against metallic K. The P3-$K_{0.45}Mn_{0.5}Co_{0.5}O_2$ nanoplatelets can reversibly host K^+ ions delivering a high capacity of 140 mAh g^{-1} in the wide voltage window of 1.2–3.9 V. Exhibiting smooth voltage profiles, it offers reasonable rate capability and cyclability, retaining over 80% capacity after 50 cycles. Involving a two-phase (P3–O3) redox mechanism, P3-$K_{0.45}Mn_{0.5}Co_{0.5}O_2$ forms robust cathode material for potassium-ion batteries. With Activated Carbon, the capacitor could provide very high energy and power densities of 43 Wh kg^{-1} and 30 kW kg^{-1}, respectively, in the voltage range of 0–3.0 V. Even at a 3-s charge–discharge rate (10 A g^{-1}), an energy density of 14.5 Wh kg^{-1} could be retained (corresponding to a power of 15 kW kg^{-1}). Also it could retain 88% of its energy density with a substantially high stability up to 30,000 cycles at 10 A g^{-1}.

1. Introduction

Developing low cost and high performing energy storage systems is required for the successful launch of electric vehicles and efficient utilization of renewable energy sources such as solar, wind, and geothermal energy [1,2]. Over the years, lithium-ion batteries (LIBs) have emerged as successful power sources for portable electronics owing to their high energy density. The exponential consumption of Li-resources

* Corresponding authors.
E-mail addresses: baskars@iisc.ac.in (B. Senthilkumar), leeys@chonnam.ac.kr (Y.-S. Lee).

https://doi.org/10.1016/j.cej.2019.02.172
Received 19 December 2018; Received in revised form 16 February 2019; Accepted 23 February 2019
Available online 25 February 2019
1385-8947/

over the past decades, their increasing cost, and non-uniform geographic distribution could impede the widespread application of Li-based energy storage devices in the future [3]. This scenario has triggered research efforts to develop more affordable and abundant alternatives with operating principles similar to those of LIBs, such as sodium-ion batteries (NIBs) and potassium-ion batteries (KIBs) [4–9]. The KIBs exhibit potential owing to the abundance of K-based resources. Both K and Na occupy 2.09 and 2.36 wt% of the earth's crust, whereas Li occupies 0.0017 wt%. Furthermore, in comparison to Na^+, K^+ ions exhibit closer negative redox potential to Li^+ (K/K^+: −2.93 V vs. Na/Na^+: −2.71 V vs. saturated hydrogen electrode in aqueous media), thereby maximizing the energy density of batteries [8]. Meanwhile, the weaker Lewis acidity of K^+ ions could provide higher mobility in liquid electrolytes to yield higher power density [3]. Irrespective of these advantages, the principal challenge lies in identifying suitable electrode materials that can (de)intercalate the larger K^+ ions (1.38 Å) vis-à-vis Li^+ (0.76 Å) and Na^+ (1.02 Å) ions [6]. In this pursuit, numerous research groups are focusing efforts on developing inexpensive, high capacity, and highly stable electrode material for KIBs [6–9]. Unlike NIBs, KIBs exhibit the advantage of using graphite as anode, forming a stable intercalation compound KC_8 and delivering a reversible capacity of 279 mAh g^{-1} [10]. In addition, several other anode materials such as hard/soft carbons, metal oxides, and organic compounds can be potentially applied [11–14].

However, developing high capacity cathode materials is necessary to realize high energy-densities in KIBs as well as potassium-ion capacitors (KICs). Layered transition metal oxides are intensely studied for application in LIBs and NIBs owing to their convenient synthesis and high energy density [15,16]. Exploring transition metal oxides, Sada et al. employed $Na_{0.84}CoO_2$ as the K^+ intercalation host to obtain a capacity of over 80 mAh g^{-1} [6]. Several other transition metal oxides such as $K_{0.5}MnO_2$ and $K_{0.6}CoO_2$ have also been reported [9,17]. However, their electrochemical performance is severely limited by the multiple structural changes, moisture attack, electrolyte reaction, and metal-ion dissolution, resulting in capacity reduction [9,17]. The combined effect of several transition metal oxides can yield improved performance of KIBs as reported for $K_xMn_{0.5}Fe_{0.5}O_2$ and $K_{0.67}Ni_{0.17}Co_{0.17}Mn_{0.66}O_2$ [18,19]. In this work, we have used this strategy to synthesize $K_{0.45}Mn_{0.5}Co_{0.5}O_2$ binary oxide (referred as KMC) using the sol–gel method. The structure and electrochemical performance of a KMC cathode for KIBs have been studied for the first time. It delivers a high capacity of 140 mAh g^{-1} with suppressed structural transitions, high rate performance, and long-term cyclic stability.

Since its first introduction in 2001, Li-ion capacitors (LICs) are considered as important energy storage and power output tool for a wide range of applications from load cranes and forklifts to hybrid electric vehicles (HEVs). Among these, application of LICs is most prominent in HEVs, where an average power density above 10 kW kg^{-1} is required [20]. A preferred hybrid capacitor contains a battery-type anode (faradaic) with a high energy-density and a capacitor-type cathode providing high power-density and cycling stability [21]. During the charging process, K^+ ions move into the electrolyte, whereas the anions (PF_6^-) in the electrolyte migrate and are adsorbed on the cathode surface (non-faradaic reaction) and viceversa [22]. Meanwhile, upside-down configurations have also been reported for LICs and NICs with battery-type cathode and capacitor-type anode with high energy and power densities [23]. Notwithstanding its improved energy density, most of the reported LICs provided low rate performance and cycling stability. Hence, developing a high-power and stable hybrid capacitor without compromising the energy density remains a challenge for the research community. Activated carbon (AC) is used as a capacitive part owing to its high surface area, reasonable electrical conductivity, tailored porosity, ecofriendly nature, and low cost. In general, these ACs exhibit high stability over 100,000 cycles [24]. Hence, the energy density can be improved by utilizing a high-performance insertion host. Developing sustainable energy-storage systems are necessary to mitigate the severe drawback of depleting lithium reserves and to enhance environmental safety. Replacing lithium with sodium and potassium will result in analogous sodium-ion (NICs) and potassium-ion capacitors (KICs) with $NaPF_6$ and KPF_6 in an organic solvent as the electrolyte and could satisfy the requirement of high-energy capacitors.

Recently, sodium-ion and potassium-ion capacitors have been gaining increasing attraction in energy-storage fields owing to their economic advantage and material abundance. Till the present, few works have been reported for KICs with preferable capacitor combinations. Fan et al utilized soft-carbon as a high capacity anode coupled with a commercial AC cathode. Although it could deliver a high energy-density, it exhibits a very low power-density of 599 W kg^{-1}, and the cycle life of 1500 is highly inferior for HEV applications [21]. Dong et al. used N-doped nano-porous graphenic carbon (NGC) as cathode and $K_2T_6O_{13}$ as anode, thereby delivering an energy density of 58.2 Wh kg^{-1} at a power density of 7200 W kg^{-1} with stability over 5000 cycles [22]. The power density and cyclic stability have to be improved adequately for practical application in hybrid electric vehicles.

In the present work, P3-$K_{0.45}Mn_{0.5}Co_{0.5}O_2$ with high capacity is explored as a suitable option for insertion host in KICs. Combining this high capacity cathode with commercial AC resulted in a novel potassium-ion capacitor with very high energy and power densities with robust stability up to 30,000 cycles.

2. Experimental section

2.1. Materials preparation

Stoichiometric amounts of potassium acetate (CH_3COOK, Sigma Aldrich, 99%), manganese acetate ($(CH_3COO)_2Mn$, Sigma Aldrich, 99%), cobalt acetate ($(CH_3COO)_2Co$, Sigma Aldrich, 99%), and citric acid ($HOC(COOH)(CH_2COOH)_2$, Sigma Aldrich, 99.5%) were dissolved completely in 100-ml distilled water with steady magnetic stirring. The excess amount of water was evaporated at 80 °C to obtain the gel precursor, which was dried at 120 °C for 12 h and calcined at 500 °C to remove the organic moieties. Finally, the powder was again ground and calcined at a high temperature (800 °C) to obtain the final product.

2.2. Material characterization

The XRD patterns of the samples were obtained over a 2θ range of 5–90° using Cu Kα radiation. Rietveld analysis was performed to determine the structural parameters after metal-ion doping. The elemental composition of the samples was analyzed using inductively coupled plasma atomic energy spectroscopy (ICP-AES). The valence state of the elements was identified using X-ray photoelectron spectroscopy (XPS). The morphology and microstructure of the samples were analyzed using field emission scanning electron microscopy (FE-SEM), selected area electron diffraction (SAED), energy dispersive spectroscopy (EDS), and high-resolution transmission electron microscopy (HRTEM).

2.3. Electrochemical measurements

For half-cell studies, each cathode consisted of 2.5 mg of the active material mixed with 0.5 mg of Ketjan black and 0.5 mg of Teflonized acetylene black (TAB) acting as binder. The slurry, obtained with the assistance of ethanol, was pressed on a stainless-steel current collector and dried in a vacuum oven at 160 °C for 4 h prior to cell fabrication. CR2032 coin type potassium half-cells were assembled inside an Ar-filled glove box employing 0.8-M KPF_6 dissolved in EC: DEC (1:1 (v/v)) solution as the electrolyte, potassium metal foil as the counter electrode, and layered $K_{0.45}Mn_{0.5}Co_{0.5}O_2$ as the working electrode. The two electrodes were separated by a porous polypropylene film (Celgard,

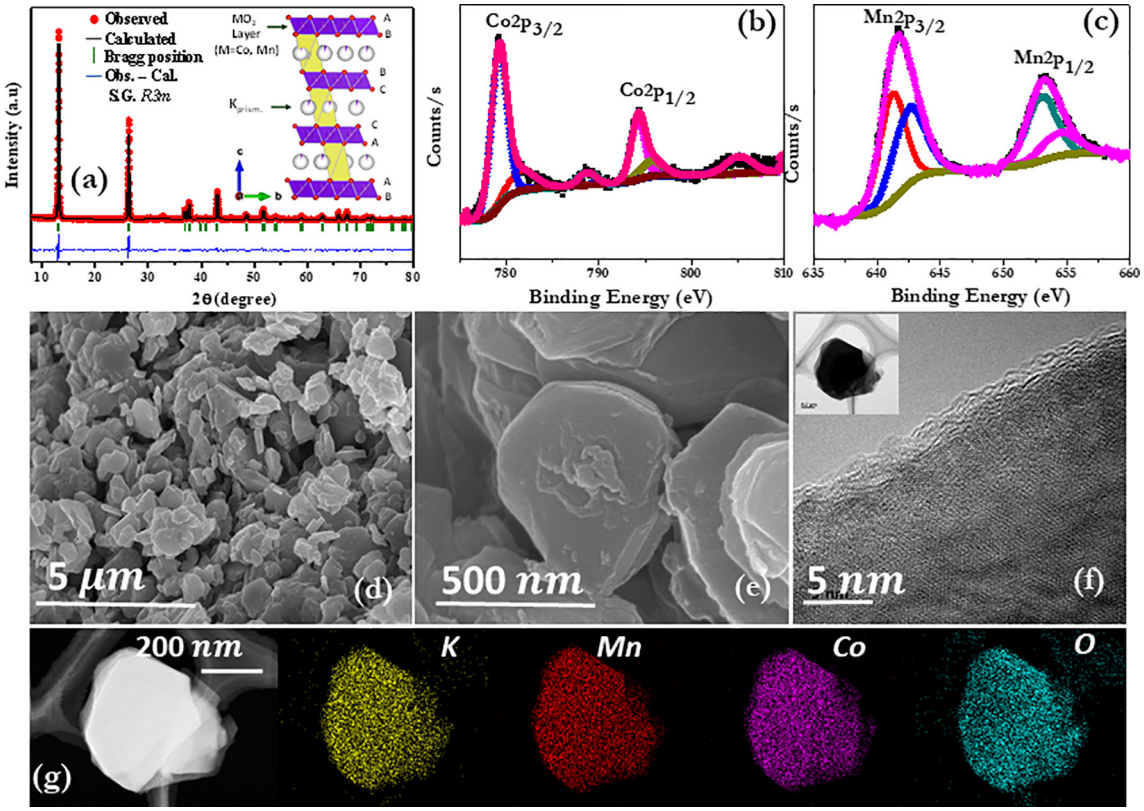

Fig. 1. (a). XRD pattern of KMC synthesized by sol–gel method. (b, c) XPS spectra of Co and Mn, respectively. (d, e) SEM images at lower and higher magnifications. (f) HRTEM image illustrating the lattice fringes (Inset) TEM image of single particle. (g) Elemental mapping of individual elements.

USA). Cyclic voltammetry, galvanostatic charge discharge, and electrochemical impedance spectroscopy were carried out for the half-cell and KIC using the Biologic SP-300 electrochemical work station (France).

3. Result and discussion

$K_{0.45}Mn_{0.5}Co_{0.5}O_2$ was prepared using citric-acid-assisted sol–gel method as described in the Supporting information. The XRD analysis verified the formation of a highly crystalline P3-type hydrated layered oxide product exhibiting a hexagonal structure with *R3m* symmetry (Fig. 1a). This P3 layered structure has oxygen atoms arranged parallel in ABBCCA sequence, wherein the Mn/Co ions occupy the octahedral units and K ions occupy the prismatic location sandwiched between the layers [9]. Using ICP-OES spectroscopy study, the K:Mn:Co elemental ratio was determined to be 0.45:0.495:0.49, matching reasonably with the final composition. The deconvoluted XPS peaks of the main elements are shown in Fig. 1(b, c)) and Fig. S1 (Supporting information). The K2p spectrum is composed of two peaks: a $K2p_{3/2}$ component and a $K2P_{1/2}$ component (Fig. S1). These two peaks are separated by an energy value of 2.68 eV, similar to other compounds with $K2p_{3/2}$ peak located at a lower binding energy [25]. The $Co2p_{3/2}$ and $Co2p_{1/2}$ peaks are deconvoluted into four peaks along with their satellite peaks. The peaks appearing at the binding energies of 779.24 and 794.24 eV are for Co^{3+} and those of 781.7 and 795.82 are for Co^{2+} [26,27]. Similarly, the Mn2p peak can be deconvoluted into four peaks. The peaks appearing at 642.49 eV and 654.31 eV denote Mn^{4+}, and the two peaks at 641.24 eV and 652.99 eV arise from Mn^{3+} [16]. The FESEM images revealed the formation of homogeneous micrometric clusters having finer 500-nm particles (Fig. 1(d, e)). The high resolution TEM image depicted the fringes exhibiting a d-spacing similar to the one measured by XRD for the (1 0 1) plane. Fig. 1g shows the energy dispersive spectroscopy (EDS) mapping of the crystallites with a homogeneous distribution of K, Mn, Co and O.

3.1. $K_{0.45}Mn_{0.5}Co_{0.5}O_2$ potassium-ion half-cell performance

The electrochemical performance of the $K_{0.45}Mn_{0.5}Co_{0.5}O_2$ cathode was studied by combining potentiodynamic cyclic voltammetry (CV), galvanostatic charge-discharge cycling (GCD), and electrochemical impedance spectroscopy (EIS) (Fig. 2). First, the charge–discharge studies were carried out at 10 mA g^{-1} between two voltage windows of 1.5–3.9 V (Fig. 2a) and 1.2–3.9 V (Fig. 2b). The high voltage operation was constrained owing to the irreversible structural changes of the layered oxides above 4.0 V [9]. The OCV for both the cells were ~2.9 V, similar to that in the earlier reported works. At the lower voltage window of 1.5–3.9 V, the initial charge/discharge capacity values were 66 mAh g^{-1} and 89 mAh g^{-1}, respectively. The potential of these cells are determined by the K^+ content and their distribution (K^+/vacancy ordering) in the layered structure [17]. Unary transition metal oxides such as K_xMnO_2 and K_xCoO_2 exhibit stepwise GCD voltage curves denoting multiple phase transitions and K^+/vacancy ordering [9,17]. This multi-step voltage profiles can be a hindrance to practical applications. In contrast, the stepwise plateaus are highly suppressed in the GCD voltage profiles of $K_{0.45}Mn_{0.5}Co_{0.5}O_2$, indicating smooth K^+ (de)intercalation. When charged to 3.9 V, five small plateaus were observed at 1.88, 2.30, 2.60, 3.14, and 3.63 V, which are highly reversible during the consecutive cycles. The plateau below 2.5 V was owing to the oxidation of Mn^{3+} to Mn^{4+} and that at 3.14 V was owing to the oxidation of Co^{3+} to Co^{4+} [28]. The extraction of K^+ ions results in a phase transition with the appearance of a plateau at 3.63 V. The peak in between 2.5 V and 3.0 V results from the K^+/vacancy ordering as reported in sodium analogues [29]. During discharge, the corresponding reduction peaks appear at 1.85, 2.25, 2.50, and 3.05 V with high reversibility. These oxidation/reduction peaks do not undergo voltage shift upon cycling, which indicates its robust chemical stability. We repeated the

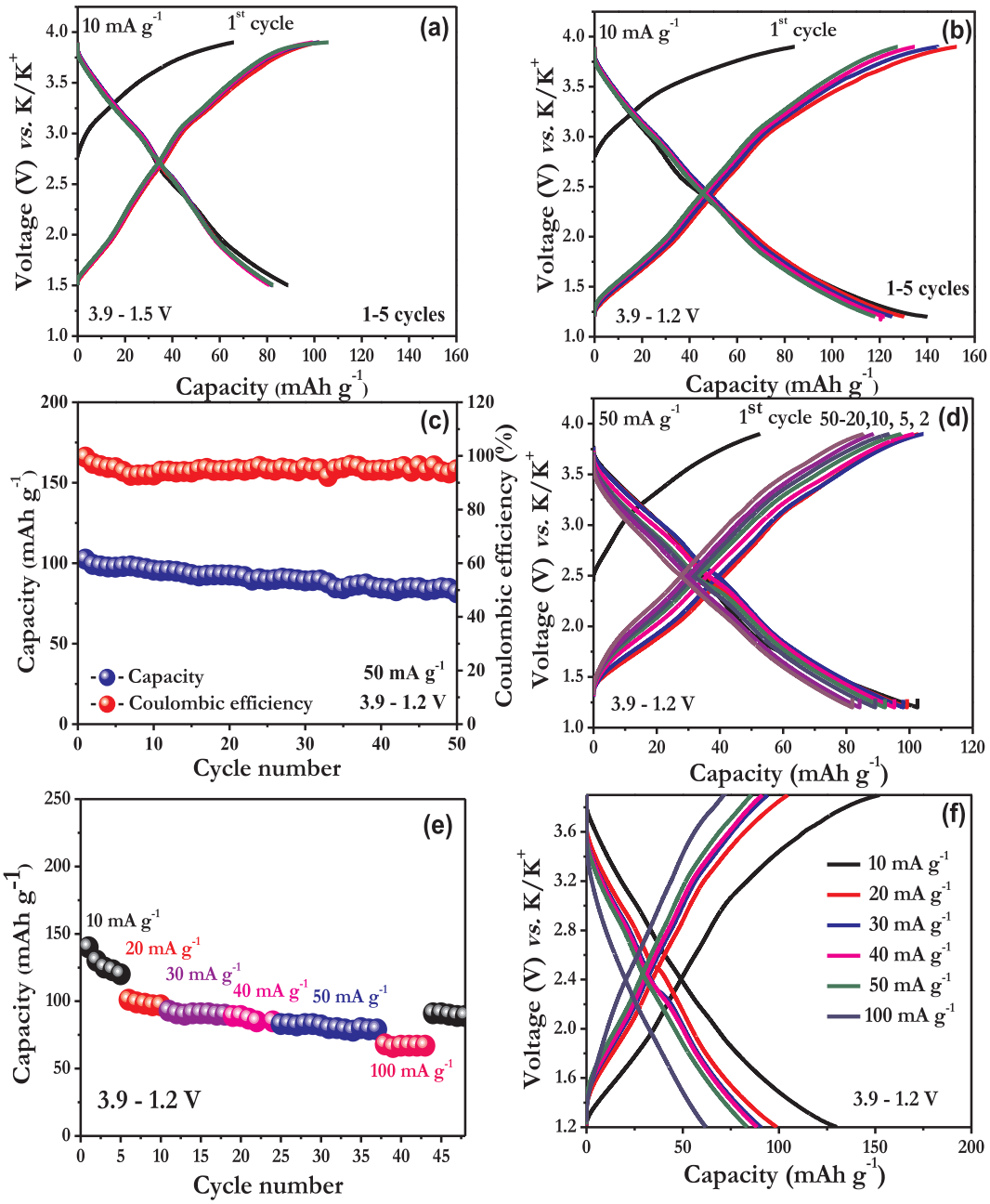

Fig. 2. (a, b). Initial charge–discharge curves at different cutoff voltages at current density of 10 mA g^{-1}. (c) Cyclic stability at 50 mA g^{-1} for 50 consecutive cycles (d) Charge–discharge curves at 50 mA g^{-1} for 50 cycles between 1.2 and 3.9 V (e, f) Rate performance and the corresponding charge–discharge curves at different current rates.

GCD analysis in the voltage window of 1.2–3.9 V for an identical current of 10 mA g^{-1}. When charged to 3.9 V, the deintercalation of K^+ ions from cathode resulted in an initial charge capacity of 65.9 mAh g^{-1}. Upon discharging to 1.2 V excess K^+ ions from the anode are intercalated back into the layered structure, delivering a capacity of 140 mAh g^{-1}. It indicates that the value of x in $K_xMn_{0.5}Co_{0.5}O_2$ varies between 0.26 and 0.56 during charge and discharge cycling. The capacity at the first charge is less than the first discharge owing to the potassium deficient structure at the initial phase. The initial charge curve was observed to be different in the subsequent cycles owing to the structural transition of the initial K^+-deficient structure upon cycling. This type of behavior has been observed in various alkali-deficient cathodes in NIBs [30]. Hence, the voltage range should be carefully optimized for superior performance. The corresponding differential capacity plot is shown in Fig. S2. Irrespective of the applied potential window, pair of redox peaks appear at 1.89, 2.30, 2.63, 3.13, 3.60 V, and at 1.83, 2.20, 2.55, and 3.09 V, respectively. However, in this case, the presence of the sharp peaks indicates a clear phase transition owing to the planar repulsion between the adjacent oxygen layers upon gradual K^+-ion deintercalation [31].

Although the operating principle of sodium and potassium-ion batteries is similar, the larger ionic size of K^+ ions hinders the realization of structural stability during long-term cycling with an extended voltage window. Fig. 2c illustrates the cyclic stability of a $K_{0.45}Mn_{0.5}Co_{0.5}O_2$ cathode for the first 50 cycles, within the extended voltage window of 1.2–3.9 V. At 50 mA g^{-1}, $K_{0.45}Mn_{0.5}Co_{0.5}O_2$ exhibits an initial capacity of 102 mAh g^{-1}. After 50 cycles, the cell could provide 82 mAh g^{-1} with a capacity retention of 80% and a very low capacity reduction of 0.4 mAh g^{-1} per cycle. Furthermore, the coulombic efficiency was observed to be significantly above 95% till 50

cycles, demonstrating the high reversibility and feasible K^+ (de)insertion pathways. The corresponding charge–discharge curves are highly sloping without any significant plateau (Fig. 2d). The material exhibits voltage fading as revealed by the widening gap between the charge–-discharge curves. Two major cathodic peaks are present at 1.84 V and 3.07 V owing to the oxidation of Mn^{3+} and Co^{3+}, and the corresponding reduction peaks appear at 1.81 V and 2.86 V. As the cycling proceeds, the cathodic peaks are shifted to a higher potential, whereas the reduction peaks are shifted to a lower potential. When charged to a high potential (above 3.2 V), a sharp phase transition occur as result of the removal of more K^+ ions. This structural transition at a higher voltage is the main cause of the capacity reduction in these layered oxides.

The rate capabilities at 10, 20, 30, 40, 50, and 100 mA g^{-1} were tested (Fig. 2e), and the corresponding charge–discharge curves are compared in Fig. 2f. The electrode delivered discharge capacities of 116, 101, 93, 89, 83, and 68 mAh g^{-1}, respectively. The capacity decreases as the current density increases because the time is inadequate for K^+-insertion into the bulk of the layered structure, and only the surface of the cathode participates in the electrochemical reaction. The presence of Co in the structure improves the kinetics of the cell [31]. Although the rate performance is higher for the K^+-ion system, it is significantly lower than those of the Li^+ and Na^+ systems owing to the higher diffusion resistance for larger K^+ ions [5]. Fig. 2f shows the charge–discharge curves at different current densities, and the relative differential capacity plots are compared in Fig. S2. The area under the plot decreases as the current rate increases, along with a reduction in the peak intensity. At a high current rate, the differential curve displays an almost capacitive-type behavior as the bulk is excluded in the reaction. Table 1 compares the performance of several reported works with ours. We evaluated the stability of the KMC electrode at high current rates of 100, 500 and 1100 mA g^{-1} in the wider voltage window of 1.2–3.9 V and represented in Fig. 3(a, b). The cathode shows superior stability with above 50% capacity retention after 150 cycles at 100 mA g^{-1}. At a higher current rate of 500 mA g^{-1} the electrode could maintain 86% of its capacity after 100 cycles. The corresponding Charge discharge curves are provided in Fig. S8(a, b). These superior rate performance of the cathode make it best suitable for high energy high power KIC.

The electrochemical performance of the P3-$K_{0.45}Mn_{0.5}Co_{0.5}O_2$ material depends on the K^+-ion intercalation and deintercalation process. The electrochemical kinetics and diffusivity of potassium (K^+) ions (D_K) can be investigated by using galvanostatic intermittent titration technique (GITT) [32–34]. We performed GITT to determine the diffusion coefficient of potassium (K^+) ions (D_K) through the electrode at a current density of 2.5 mA g^{-1} within a voltage range of 1.2–3.9 V, as shown in Fig. 1. A current was applied for 60 min per titration during the discharge–charge process, with an open-circuit stand for 60 min to permit the cell potential to attain a new steady-state potential. The chemical diffusion coefficient (D_K) was calculated by assuming that the potassium diffusion in the electrode obeys Fick's law

$$D_{K^+} = \frac{4}{\pi\tau}\left(\frac{m_B V_M}{M_B A}\right)^2\left(\frac{\Delta E_s}{\tau(dE_\tau / d\sqrt{\tau})}\right)^2 \quad (\tau \ll L^2/D) \tag{1}$$

where m_B is the electrode active mass; M_B is the molar mass of the electrode material; V_M is the molar volume; S is the geometric area of the electrode; M_B/V_M is obtained from the density of P3-$K_{0.45}Mn_{0.5}Co_{0.5}O_2$, which is ca. 3.8 g cm^{-3}; and L is the average thickness of the electrode. Detailed definitions of the parameters in the equation, including E_0, E_S, τ, t_0, $t_{0+\tau}$, E_τ, ΔE_S, and ΔE_τ in the GITT potential profiles, are provided in Fig. S(5–7). If the cell voltage is linearly proportional to $\tau^{1/2}$, Eq. (1) can be further simplified as

$$D_{K^+} = \frac{4}{\pi\tau}\left(\frac{m_B V_M}{M_B A}\right)^2\left(\frac{\Delta E_s}{\Delta E_\tau}\right)^2 \tag{2}$$

The calculated diffusion coefficient (D_K) is 5.6936×10^{-11} cm^2 s^{-1} at a charging potential of 3.05 V. There is no previous report for D_K in P3-$K_{0.45}Mn_{0.5}Co_{0.5}O_2$ [34]; however, this calculated value of D_K is consistent with that of $Na_{0.34}K_{0.5}CoO_2$ and superior to the case of MoS_2 (3.4×10^{-16} cm^2 s^{-1}) [6,38]. The higher values of D_K demonstrates the rapid K^+ extraction/insertion into the P3-$K_{0.45}Mn_{0.5}Co_{0.5}O_2$ particles.

To further understand the kinetics of the electrode, cyclic voltammetry was carried out in the voltage range of 1.2–3.9 V at 0.2 mV s^{-1} for 10 consecutive cycles (Fig. S3a). Two sets of redox peaks appeared owing to the Mn^{4+}/Mn^{3+} and Co^{4+}/Co^{3+} redox activity over the entire voltage window. The peaks were shifted in the consequent cycles owing to voltage polarization and structural transition [28]. To understand the kinetics of the cell, EIS was performed before and after cycling at 50 mA g^{-1}, as shown in Fig. S3b. There is a semicircle from the higher to the low frequency region followed by a sloping line in the low frequency region. The diameter of the semicircle represents the charge transfer resistance (R_{ct}), and the slope is related to the Warburg resistance owing to the K^+ ion diffusion in the cathode material [4]. After 50 cycles, the R_{ct} value of the electrode increased abruptly when compared to the first cycle owing to the structural change and degraded electrode–electrolyte contact during deeper discharge [5]. Phase transition at different voltages can exert significant impact on the electrochemical performance. To probe this effect of K^+ intercalation on the structure of KMC, we acquired XRD patterns after charging and discharging by carefully removing the cathode materials from the half-

Table 1
Comparison of this work with other reported potassium-ion battery cathodes.

Cathode	Synthesis method	Voltage (V) vs. K/K^+	Current (mA)	Capacity (mAh g^{-1})	Capacity retention
P2-$Na_{0.84}CoO_2$ [6]	Solution combustion	2.0–4.2	C/20	82	80% after 50 cycles at C/10 rate
P2-$K_{0.6}CoO_2$ [3]	Self-template method	1.7–4.0	10	82	87% after 300 cycles for 40 mA
P2-K_xCoO_2 and P3-K_xCoO_2 [7]	Solid state	2.0–3.9	11.8	60	Above 95% after 30 cycles
P2-$K_{0.6}CoO_2$[17]	Solid state	1.5–4.0	10	70	60% after 120 cycles at 100 mA g^{-1}
P3-$K_{0.5}MnO_2$ [9].	Solid state	1.5–3.9	20	100	70% after 50 cycles
$K_{0.67}Ni_{0.17}Co_{0.17}Mn_{0.66}O_2$[19]	Co-precipitation method	2.0–4.3	20	76.5	87% after 100 cycles
$K_{0.7}Mn_{0.5}Fe_{0.5}O_2$ [39]	Spray drying method	1.5–4.0	20	178	70% after 45 cycles
P3-$K_{0.45}Mn_{0.5}Co_{0.5}O_2$ (This work)	Sol–gel	1.2–3.9	10	140	80% after 50 cycles at 50 mA g^{-1} (THIS WORK)
$K_3V_2(PO_4)$ [40]	Sol–gel method	2.5–4.3	20	54	96% after 100 cycles
$KVPO_4F$ and $KVOPO_4$[41]	Sol–gel method	2.0–4.8	c/20	70	Above 90% after 50 cycles
$K_xFeFe(CN)_6{\cdot}nH_2O$[42]	Precipitation method	2.0–4.5	20	110	81% after 100 cycles
$K_{1.7}Fe[Fe(CN)_6]_{0.9}$ [43]	Solution method	2.0–4.5	10	140	85% after 100 cycles at 100 mA
FeHCF [44]	Solution method	1.5–4.0	62.5	124	96.5% After 100
Potassium ferrous ferricyanide [45]	hydrothermal	2.0–4.5	10	118.7	94% After 100 cycles at 10 mA
Anthraquinone 1,5-disulphonic acid sodium salt [46]	As prepared	1.4–3.0	0.1c	114.9	68% after 100 cycles at 0.1 C

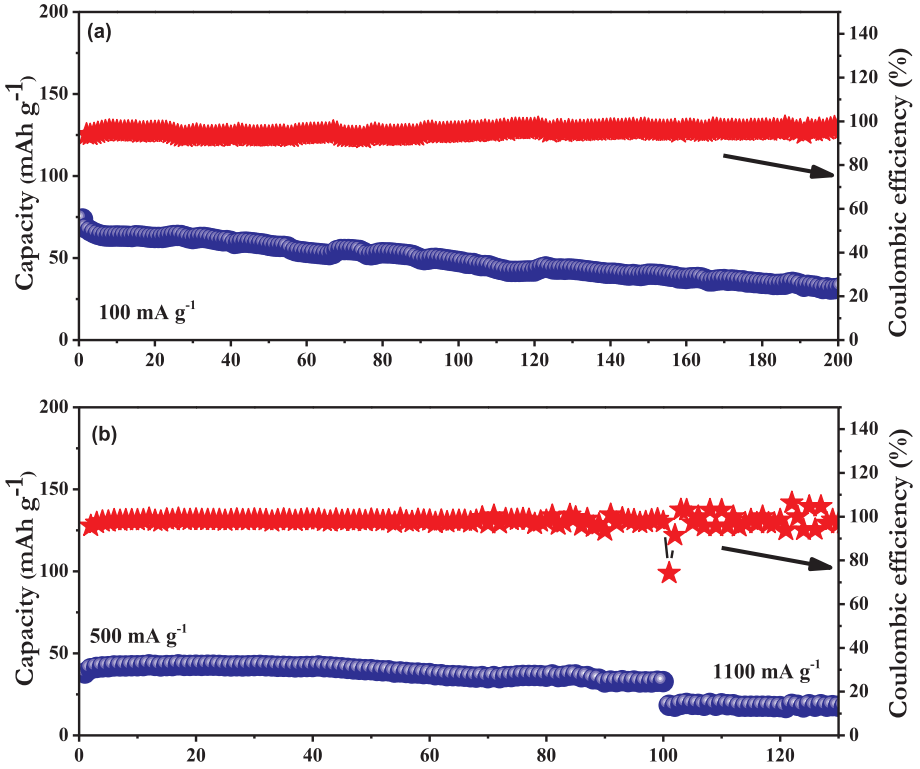

Fig. 3. Cyclic stability of KMC at different current densities (a) 100 mA g^{-1}. (b) 500 and 1100 mA g^{-1}.

cells. Fig. S3(c, d) compares the XRD patterns of the pristine, charged, and 50-cycle discharged cathode. It is evident that only two-phase reaction occurs in the $K_{0.45}Mn_{0.5}Co_{0.5}O_2$ when the value of x is in the range of $0.26 < x < 0.56$. When the electrode is charged to a higher voltage (3.9 V), the major peaks are shifted toward a lower angle owing to the increase in the d-spacing of the MeO_2 layers because of O_2– repulsion between the adjacent layers. This behavior is common to other alkali layered oxides reported till the present [31]. In addition to this peak shift, a new peak appears at $2\theta = 18.5°$ referring to the formation of O3 type structure from P3 structure [35–37]. After a 50-cycles, when discharged back to 1.5 V, the original peaks are partially restored, and their intensities are similar to that of the pristine electrode. Thus, $K_{0.45}Mn_{0.5}Co_{0.5}O_2$ could maintain reasonable stability as a cathode for KIBs even after 50 cycles. A detailed report on the P3–O3 structural variation and redox mechanism of $K_{0.45}Mn_{0.5}Co_{0.5}O_2$ cathode will be presented in the near future.

3.2. $K_{0.45}Mn_{0.5}Co_{0.5}O_2$-commercial activated carbon hybrid capacitor

Next, the electrochemical performance of a KMC electrode with hybrid supercapacitor architecture was studied. For this, the anodic performance of commercial activated carbon (CAC) was studied at a current rate of 100 mA g^{-1} between the potential windows of 1.0–3.0 V vs. K^+/K for 100 consecutive cycles. The linear charge–discharge curves symbolize the electric double layer formation during the adsorption–desorption of PF_6^- ions. An initial capacity of 35 mAh g^{-1} could be reasonably preserved until 100 cycles, indicating the robust adsorption desorption over the applied potential range. Further we cycled in the lower voltage window between 0 and 3 V at higher current rates (Fig. S9). Still the anode could show EDLC behavior with sloping voltage profile. This confirms the suitability of CAC for high power KIC.

The full cell of potassium-ion capacitors were assembled using $K_{0.45}Mn_{0.5}Co_{0.5}O_2$ as cathode and commercial activated carbon as anode. The mass of the cathode and anode are adequately balanced as per their different working potentials so as to obtain higher energy/power output. As per the capacity obtained from the cathode and anode half-cell studies against K metal as anode, the optimized mass ratio of cathode to anode for this work is 1:2. During the charging process, K^+ ions are extracted from the layered oxide structure into the electrolyte and back into the structure during the consecutive discharge ensuring higher energy density. Simultaneously the PF_6^- ions get adsorbed and desorbed on the surface of CAC electrode forming the electrical double layer resulting in higher power density [21]. The mass ratio between the cathode and anode has to be balanced to compensate the charge imbalance between them. Here the mass ratio of cathode and anode is 1:2 [47]. The optimized composition provides a higher energy–power combination with substantially high stability in the potential range of 0–3.0 V without side reactions and oxidative decomposition of the electrolyte [49]. If the operating potential of the active material exceeds the lower or upper cutoff limit, it initiates a side reaction between the electrode and electrolyte [48]. Fig. 4a shows the CV curves of the KICs for the different scan rates in the range 2–20 mV s^{-1}, exhibiting well-maintained shapes. The quasi-rectangular CV curves define the contribution of both the faradaic and non-faradaic charge storage mechanisms in the combined system [49].

Fig. 4b–d shows the typical charge–discharge curves at different current densities. Irrespective of the diffusion-regulated process, the curve resembles an ideal supercapacitor owing to its rapid charge storage kinetics [49]. The negligible IR-decrease indicates a higher electrical conductivity resulting from the advanced composition of the cathode material with the presence of binary transition metals, optimized mass balance, and potential window [50,51]. The specific capacitance of $K_{0.45}Mn_{0.5}Co_{0.5}O_2$//AC is calculated using the following relationship:

$$C_{SP}\,(\mathrm{F\ g^{-1}}) = \frac{i\,(\mathrm{mA\ g^{-1}}) \times t\,(\mathrm{s})}{\Delta v\,(\mathrm{mV})} \tag{3}$$

where $C_{SP}\,(F\ g^{-1})$ is the specific capacitance of the full cell, i is the input current measured by considering the total mass of the active material in the cathode and anode (mA g^{-1}), t is the time of the discharge curve in seconds (s), and Δv is the voltage window of the cell [51]

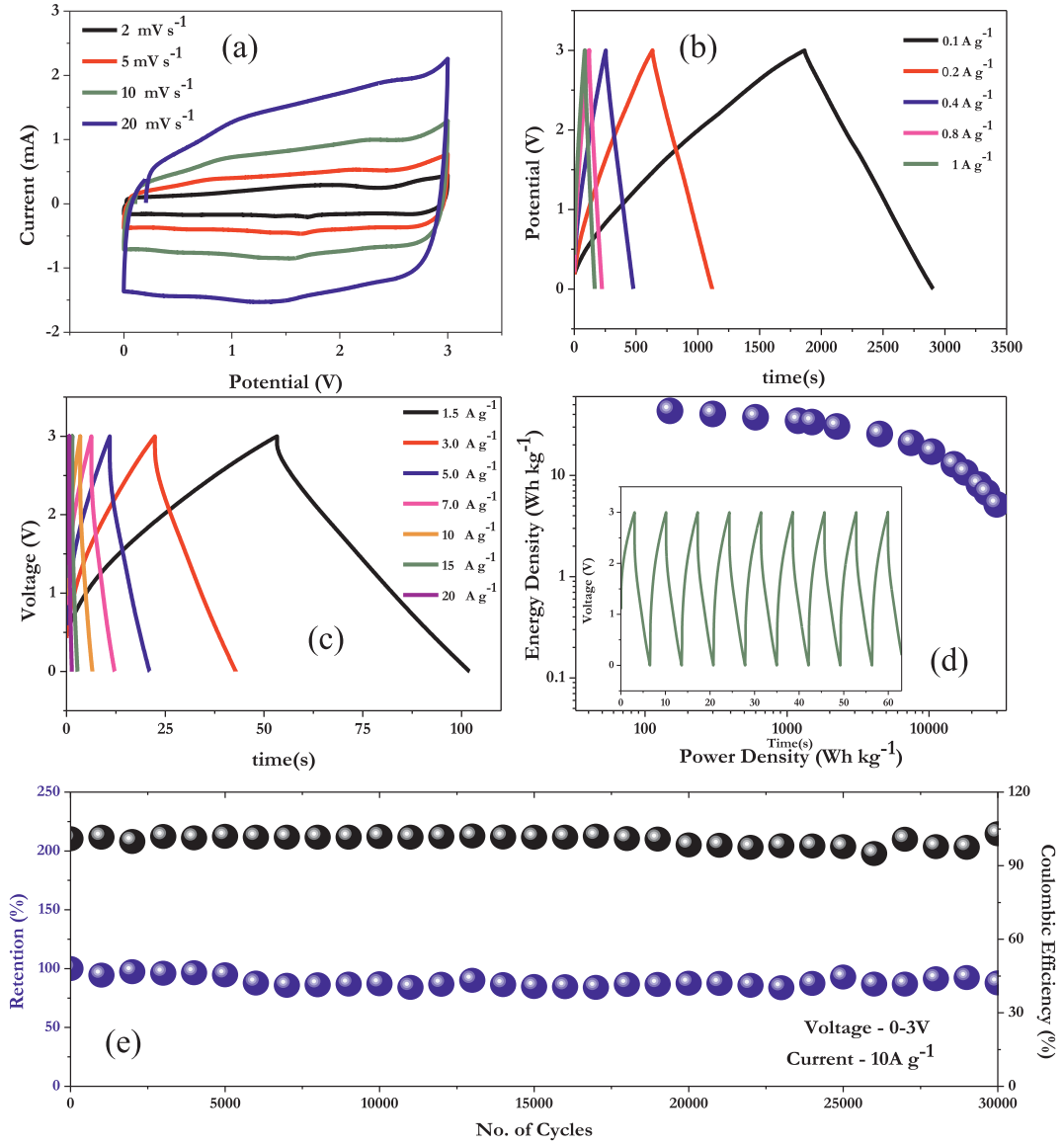

Fig. 4. (a) CV curves of KMCO//CAC hybrid capacitor at different scan rates for 0–3 V. (b, c) Charge–discharge curves of KMCO//CAC hybrid capacitor for varying current densities. (d) Ragone plot of KIC. Inset is the first few cycles obtained at a current density of 10 A g^{-1} (e) Cyclic performance of KIC at 10 A g^{-1} up to 30,000 cycles (0–3 V).

$$ED(\text{Wh kg}^{-1}) = \frac{C_{SP} \times V^2}{7.2} \quad (4)$$

$$PD(\text{W kg}^{-1}) = \frac{ED(\text{Wh kg}^{-1}) \times 3600}{t(\text{s})} \quad (5)$$

The KIC delivers the highest specific capacitance of 34.69 F g^{-1} at the current density of 0.1 A g^{-1}, considering the active masses of both the cathode and anode. At high currents also, the CD curves exhibit negligible IR-loss, demonstrating the superior kinetics of the well-balanced KIC. Fig. 4d illustrates the Ragone plot of the fabricated hybrid capacitor. The energy and power density of the supercapacitor is calculated by considering the active masses of both the cathode and anode using the formulae in Eq. (2) and (3).

The full cell delivered a very high energy density of 43.37 Wh kg^{-1} corresponding to the power density of 150 W kg^{-1} (input current = 0.1 A g^{-1}). Even at a substantially high power density of 30 kW kg^{-1} (it corresponds to 0.62 s for discharge), the full cell could retain 5.16 Wh kg^{-1}. When compared to similar unconventional combinations of hybrid capacitors in which the cathode is of battery-type material and the anode is of non-faradaic type, the high energy density was comparable to the commercial lithium hybrid capacitors along with superior power density among rival supercapacitors. For comparison, the reported values of lithium- and sodium-ion capacitors are tabulated together with those of our work (Table S1). The high energy and power characteristics of the proposed potassium-ion hybrid capacitor can be ascribed to the (i) high capacity resulting from the unique composition of $K_{0.45}Mn_{0.5}Co_{0.5}O_2$ when used as a cathode in potassium-ion batteries (the partial replacement of Mn with Co improves the structural stability of the cathode; moreover, the Co undergoes reduction and oxidation in parallel with Mn, contributing toward higher capacity), (ii) suppression of alkali ion ordering and the resulting structural heterogeneity, which causes a smooth voltage profile owing to the co-existence of Mn and Co in the lattice structure, (iii) enhanced ionic conductivity owing to the presence of cobalt, and (iv) formation of nano-sized particles exhibiting shorter ion diffusion length and charge transfer resistance [52–55].

For the successful application of hybrid supercapacitors in HEVs, long-term cycling and high power delivery is necessary with energy density comparable to that of lead–acid batteries [20]. Based on the above results, we intended to test the cyclic stability of the device at a substantially high current rate of 10 A g^{-1} (Fig. 4e). As expected, the

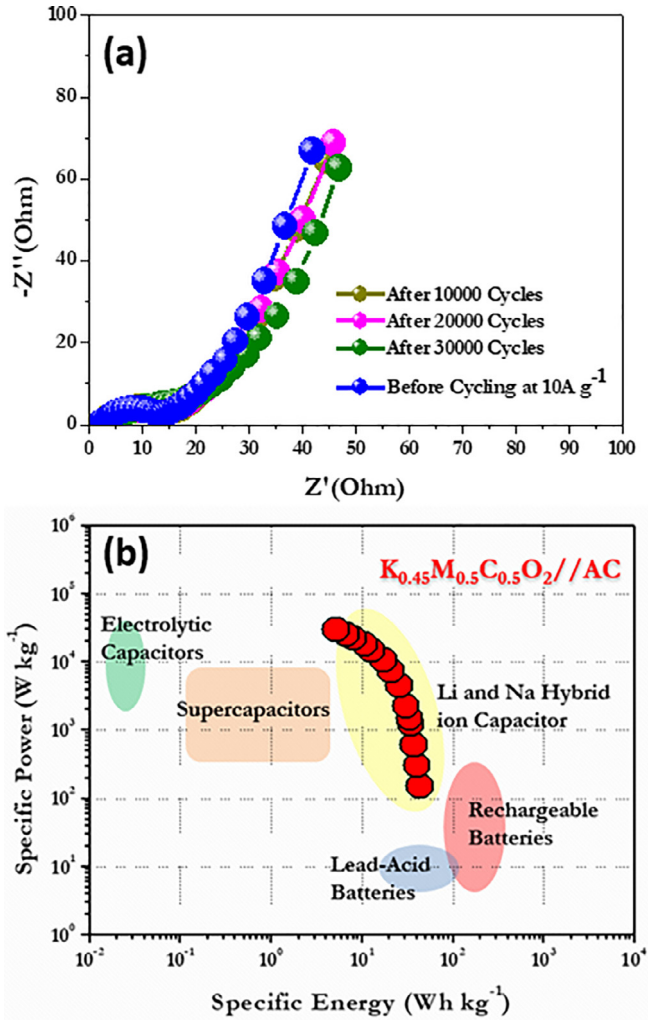

Fig. 5. (a) Nyquist plot of KIC before and after cycling at intermediate intervals, (b) Ragone plot of KIC compared with other commercial energy storage devices.

cell could effectively preserve the initial energy density of 12.85 Wh kg^{-1} after 30,000 cycles, retaining 87.8% of its initial energy density (11.3 Wh kg^{-1}) with 100% coulombic efficiency and a marginal degradation rate of 0.0004% per cycle. This performance could surpass all reported potassium-based hybrid capacitors (less than 5000 cycles) and a few highly popular sodium-ion hybrid capacitors (Table S1). The inset in the Fig. 4d shows the initial cycling curves at 10 A g^{-1}, depicting near-linear behavior without IR-decrease. To our knowledge, the cyclic stability of our work is higher than those of most of the reported layered lithium- and sodium-ion capacitors. Furthermore, this remarkable stability is verified using the Nyquist plot (Fig. 5a) obtained before and after cycling for 30,000 cycles at a high current rate. A semicircle in the high frequency region is followed by a sloping line at lower frequencies. The former corresponds to the charge transfer resistance, and the latter is diffusion-related impedance. The negligible change in the charge transfer resistance clearly indicates the stability of cathode even after continuous interaction with the electrolyte species [56]. This was supported by the Ex-situ SEM of the KMC electrode before cycling, after 10,000 cycles, and after 30,000 cycles in Fig S10(a–f). The morphology of the microparticles were well preserved even after 30,000 cycles at 10 A g^{-1}. Fig. 5(b) demonstrates the superiority of this new system over other energy storage devices reported till the present.

4. Conclusions

In summary, we propose P3-$K_{0.45}Mn_{0.5}Co_{0.5}O_2$ as a new robust cathode for potassium-ion batteries. This binary cathode delivers a high capacity of 140 mAh g^{-1} involving both Mn^{4+}/Mn^{3+} and Co^{4+}/Co^{3+} redox activities, exhibiting an average operating potential of 2.55 V (vs. K/K^+). With the K content varying from 0.26 to 0.56, it delivers adequate cycling stability and rate kinetics. The presence of binary (Mn–Co) transition metals in the structure suppresses the K^+/vacancy ordering, resulting in smooth charge and discharge curves. Ex situ X-ray diffraction and electrochemical analysis indicated a two-phase (P3–O3) reaction during the charge/discharge process. It could retain 80% of its initial capacity after 50 cycles. This sets a benchmark for the potential application of Co–Mn binary cathode for potassium-ion batteries. As a cathode for a potassium-ion hybrid capacitor, the new configuration could deliver the highest energy (43 Wh kg^{-1}) and power density (30 kW kg^{-1}) in conjunction with remarkable stability over 30,000 cycles, thereby making it a potentially highly-preferred system for future HEV applications.

Acknowledgements

The authors gratefully acknowledge the financial support from the National Research Foundation of Korea(NRF) grant funded by the Korean government (Ministry of Science, ICT & Future Planning) (No. 2016R1A4A1012224). B.S. thanks DST (SERB), India for providing the National Postdoctoral Fellowship (PDF/2015/00217). P.B. thanks the Department of Atomic Energy for financial support in form of a DAE-BRNS Young Scientist Research Award.

Appendix A. Supplementary data

Supplementary data to this article can be found online at https://doi.org/10.1016/j.cej.2019.02.172.

References

[1] F. Bonaccorso, L. Colombo, G. Yu, M. Stoller, V. Tozzini, A.C. Ferrari, R.S. Ruoff, V. Pellegrini, Graphene related two-dimensional crystals, and hybrid systems for energy conversion and storage, Science 347 (2015) 1246507.
[2] J.W. Choi, D. Aurbach, Promise and reality of post-lithium-ion batteries with high energy densities, Nat. Rev. Mater. 1 (2016) 16013.
[3] T. Deng, X. Fan, C. Luo, J. Chen, L. Chen, S. Hou, N. Eidson, X. Zhou, C. Wang, Self-templated formation of P2-type $K_{0.6}CoO_2$ microspheres for high reversible potassium-ion batteries, Nano Lett. 18 (2018) 1522–1529.
[4] H.V. Ramasamy, K. Kaliyappan, R. Thangavel, V. Aravindan, K. Kang, D.U. Kim, Y. Park, X. Sun, Y.S. Lee, Cu-doped P2-$Na_{0.5}Ni_{0.33}Mn_{0.67}O_2$ encapsulated with MgO as a novel high voltage cathode with enhanced Na-storage properties, J. Mater. Chem. A 5 (2017) 8408–8415.
[5] Y. Zhu, X. Qi, X. Chen, X. Zhou, X. Zhang, J. Wei, Y. Hu, Z. Zhou, A P2-$Na_{0.67}Co_{0.5}Mn_{0.5}O_2$ cathode material with excellent rate capability and cycling stability for sodium ion batteries, J. Mater. Chem. A 4 (2016) 11103–11109.
[6] K. Sada, B. Senthilkumar, P. Barpanda, Electrochemical potassium-ion intercalation in Na_xCoO_2: a novel cathode material for potassium-ion batteries, Chem. Commun. 53 (2017) 8588–8591.
[7] Y. Hironaka, K. Kubota, S. Komaba, P2- and P3-K_xCoO_2 as an electrochemical potassium intercalation host, Chem. Commun. 53 (2017) 3693–3696.
[8] B. Tian, W. Tang, K. Leng, Z. Chen, S.J.R. Tan, C. Peng, G.-H. Ning, W. Fu, C. Su, G.W. Zheng, Phase transformations in TiS_2 during K intercalation, ACS Energy Lett. 2 (2017) 1835–1840.
[9] H. Kim, D.H. Seo, J.C. Kim, S.H. Bo, L. Liu, T. Shi, G. Ceder, Investigation of potassium storage in layered P3-type $K_{0.5}MnO_2$ cathode, Adv. Mater. 29 (2017) 1702480.
[10] Z. Jian, W. Luo, X. Ji, Carbon electrodes for K-ion batteries, J. Am. Chem. Soc. 137 (2015) 11566–11569.
[11] Z. Xing, Z. Jian, W. Luo, Y. Qi, C. Bommier, E.S. Chong, Z. Li, L. Hu, X. Ji, A perylene anhydride crystal as a reversible electrode for K-ion batteries, Energy Storage Mater. 2 (2016) 63–68.
[12] X. Wang, K. Han, D. Qin, Q. Li, C. Wang, C. Niu, L. Mai, Polycrystalline soft carbon semi-hollow microrods as anode for advanced K-ion full batteries, Nanoscale 9 (2017) 18216–18222.
[13] C. Chen, Z. Wang, B. Zhang, L. Miao, J. Cai, L. Peng, Y. Huang, J. Jiang, Y. Huang, L. Zhang, Nitrogen-rich hard carbon as a highly durable anode for high-power potassium-ion batteries, Energy Storage Mater. 8 (2017) 161–168.

[14] J. Han, M. Xu, Y. Niu, G.-N. Li, M. Wang, Y. Zhang, M. Jia, C. Li, Exploration of $K_2Ti_8O_{17}$ as an anode material for potassium-ion batteries, Chem. Commun. 52 (2016) 11274–11276.

[15] P.K. Nayak, J. Grinblat, M. Levi, E. Levi, S. Kim, J.W. Choi, D. Aurbach, Al doping for mitigating the capacity fading and voltage decay of layered Li and Mn-rich cathodes for Li-ion batteries, Adv. Energy Mater. 6 (2016) 1502398.

[16] H.V. Ramasamy, K. Kaliyappan, R. Thangavel, W.M. Seong, K. Kang, Z. Chen, Y.S. Lee, Efficient method of designing stable layered cathode material for sodium ion batteries using aluminum doping, J. Phys. Chem. Lett. 8 (2017) 5021–5030.

[17] H. Kim, J.C. Kim, S.H. Bo, T. Shi, D.H. Kwon, G. Ceder, K-ion batteries based on a P2-type $K_{0.6}CoO_2$ cathode, Adv. Energy Mater. 7 (2017) 1700098.

[18] X. Wang, P. Hu, C. Niu, J. Meng, X. Xu, X. Wei, C. Tang, W. Luo, L. Zhou, Q. An, New-type $K_{0.7}Fe_{0.5}Mn_{0.5}O_2$ cathode with an expanded and stabilized interlayer structure for high-capacity sodium-ion batteries, Nano Energy 35 (2017) 71–78.

[19] C. Liu, S. Luo, H. Huang, Z. Wang, A. Hao, Y. Zhai, Z. Wang, $K_{0.67}Ni_{0.17}Co_{0.17}Mn_{0.66}O_2$: a cathode material for potassium-ion battery, Electrochem. Commun. 82 (2017) 150–154.

[20] Z. Jian, V. Raju, Z. Li, Z. Xing, Y.S. Hu, X. Ji, A high-power symmetric na-ion pseudocapacitor, Adv. Funct. Mater. 25 (2015) 5778–5785.

[21] L. Fan, K. Lin, J. Wang, R. Ma, B. Lu, A Nonaqueous potassium-based battery-supercapacitor hybrid device, Adv. Mater. 30 (2018) 1800804.

[22] S. Dong, Z. Li, Z. Xing, X. Wu, X. Ji, X. Zhang, A novel potassium-ion hybrid capacitor based on an anode of $K_2Ti_6O_{13}$ micro-scaffolds, ACS Appl. Mater. Interfaces 10 (2018) 15542–15547.

[23] K. Karthikeyan, S. Amaresh, K.J. Kim, S.H. Kim, K.Y. Chung, B.W. Cho, Y.S. Lee, A high performance hybrid capacitor with Li_2CoPO_4F cathode and activated carbon anode, Nanoscale 5 (2013) 5958–5964.

[24] I. Plitz, A. Dupasquier, F. Badway, J. Gural, N. Pereira, A. Gmitter, G.G. Amatucci, The design of alternative nonaqueous high power chemistries, Appl. Phys. A: Mater. Sci. Process. 82 (2006) 615–626.

[25] R. Sawyer, H.W. Nesbitt, R.A. Secco, High resolution X-ray photoelectron spectroscopy (XPS) study of K_2O-SiO_2 glasses: evidence for three types of O and at least two types of Si, J. Non. Cryst. Solids 358 (2012) 290–302.

[26] S. Xie, Y. Liu, J. Deng, J. Yang, X. Zhao, Z. Han, K. Zhang, H. Dai, Insights into the active sites of ordered mesoporous cobalt oxide catalysts for the total oxidation of O-xylene, J. Catal. 352 (2017) 282–292.

[27] P. Mountapmbeme Kouotou, H. Vieker, Z.Y. Tian, P.H. Tchoua Ngamou, A. El Kasmi, A. Beyer, A. Gölzhäuser, K. Kohse-Höinghaus, Structure-activity relation of spinel-type Co-Fe oxides for low-temperature CO oxidation, Catal. Sci. Technol. 4 (2014) 3359–3367.

[28] Y. Bai, L. Zhao, C. Wu, H. Li, Y. Li, F. Wu, Enhanced sodium ion storage behavior of P2-type $Na_{2/3}Fe_{1/2}Mn_{1/2}O_2$ synthesized via a chelating agent assisted route, ACS Appl. Mater. Interfaces 8 (2016) 2857–2865.

[29] P. Wang, Y. You, Y. Yin, Y. Guo, An O3-type $NaNi_{0.5}Mn_{0.5}O_2$ cathode for sodium-ion batteries with improved rate performance and cycling stability, J. Mater. Chem. A 4 (2016) 17660–17664.

[30] I. Hasa, D. Buchholz, S. Passerini, B. Scrosati, J. Hassoun, High performance $Na_{0.5}[Ni_{0.23}Fe_{0.13}Mn_{0.63}]O_2$ cathode for sodium-ion batteries, Adv. Energy Mater. 4 (2014) 1400083.

[31] L.G. Chagas, D. Buchholz, C. Vaalma, L. Wuab, S. Passerini, P-type $Na_xNi_{0.22}Co_{0.11}Mn_{0.66}O_2$ materials: linking synthesis with structure and electrochemical performance, J. Mater. Chem. A 2 (2014) 20263–20270.

[32] W. Weppner, R.A. Huggins, Determination of the kinetic parameters of mixed conducting electrodes and application to the system Li_3Sb, J. Electrochem. Soc. 124 (1977) 1569.

[33] Z. Jian, Z. Xing, C. Bommier, Z. Li, X. Ji, Hard carbon microspheres: potassium ion anode vs sodium ion anode, Adv. Energy Mater. 6 (2016) 1501874.

[34] Y. Zhu, T. Gao, X. Fan, F. Han, C. Wang, Electrochemical techniques for intercalation electrode materials in rechargeable batteries, Acc. Chem. Res. 50 (2017) 1022.

[35] R. Berthelot, D. Carlier, C. Delmas, Electrochemical investigation of the P2–Na_xCoO_2 phase diagram, Nat. Mater. 10 (2011) 74–80.

[36] S. Komaba, N. Yabuuchi, T. Nakayama, A. Ogata, T. Ishikawa, I. Nakai, Study on the reversible electrode reaction of $Na_{1-x}Ni_{0.5}Mn_{0.5}O_2$ for a rechargeable sodium-ion battery, Inorg. Chem. 51 (2012) 6211–6220.

[37] S.H. Bo, X. Li, A.J. Toumar, G. Ceder, Layered-to-rock-salt transformation in desodiated Na_xCrO_2(x = 0.4), Chem. Mater. 28 (2016) 1419–1429.

[38] X. Ren, Q. Zhao, W.D. McCulloch, Y. Wu, MoS_2 as a long life host material for potassium ion intercalation, Nano Res. 10 (2017) 1313.

[39] X. Wang, X. Xu, C. Niu, J. Meng, M. Huang, X. Liu, Z. Liu, L. Mai, Earth abundant Fe/Mn-based layered oxide interconnected nanowires for advanced k-ion full batteries, Nano Lett. 17 (2017) 544–550.

[40] J. Han, G.N. Li, F. Liu, M. Wang, Y. Zhang, L. Hu, C. Dai, M. Xu, Investigation of $K_3V_2(PO_4)_3$/C nanocomposites as high-potential cathode materials for potassium-ion batteries, Chem. Commun. 53 (2017) 1805–1808.

[41] K. Chihara, A. Katogi, K. Kubota, S. Komaba, $KVPO_4F$ and $KVOPO_4$ toward 4 volt-class potassium-ion batteries, Chem. Commun. 53 (2017) 5208–5211.

[42] X. Wu, Z. Jian, Z. Li, X. Ji, Prussian white analogues as promising cathode for non-aqueous potassium-ion batteries, Electrochem. Commun. 77 (2017) 54–57.

[43] G. He, L.F. Nazar, Crystallite size control of Prussian white analogues for nonaqueous potassium-ion batteries, ACS Energy Lett. 2 (2017) 1122–1127.

[44] Z. Shadike, D.R. Shi, T. Wang, M.H. Cao, S.F. Yang, J. Chen, Z.W. Fu, Long life and high-rate berlin green $FeFe(CN)_6$ cathode material for a non-aqueous potassium-ion battery, J. Mater. Chem. A 5 (2017) 6393–6398.

[45] S. Chong, Y. Chen, Y. Zheng, Q. Tan, C. Shu, Y. Liu, Z. Guo, Potassium ferrous ferricyanide nanoparticles as a high capacity and ultralong life cathode material for nonaqueous potassium-ion batteries, J. Mater. Chem. A 5 (2017) 22465–22471.

[46] J. Zhao, J. Yang, P. Sun, Y. Xu, Sodium sulfonate groups substituted anthraquinone as an organic cathode for potassium batteries, Electrochem. Commun. 86 (2018) 34–37.

[47] Y.E. Zhu, L. Yang, J. Sheng, Y. Chen, H. Gu, J. Wei, Z. Zhou, Fast sodium storage in TiO_2@CNT@C nanorods for high-performance Na-ion capacitors, Adv. Energy Mater. 7 (2017) 1701222.

[48] R. Ding, L. Qi, H. Wang, An investigation of spinel $NiCo_2O_4$ as anode for Na-ion capacitors, Electrochim. Acta 114 (2013) 726–732.

[49] Q. Xia, H. Yang, M. Wang, M. Yang, Q. Guo, L. Wan, H. Xia, Y. Yu, High energy and high power lithium-ion capacitors based on boron and nitrogen dual-doped 3D carbon nanofibers as both cathode and anode, Adv. Energy Mater. 7 (2017) 1701336.

[50] Z. Chen, V. Augustyn, X. Jia, Q. Xiao, B. Dunn, Y. Lu, High-performance sodium-ion pseudocapacitors based on hierarchically porous nanowire composites, ACS Nano 6 (2012) 4319–4327.

[51] S. Birgisson, Y. Shen, B.B. Iversen, In operando observation of sodium ion diffusion in a layered sodium transition metal oxide cathode material, P2 $Na_xCo_{0.7}Mn_{0.3}O_2$, Chem. Commun. 53 (2017) 1160–1163.

[52] J.-H. Cheng, C.-J. Pan, J.-F. Lee, J.-M. Chen, M. Guignard, C. Delmas, D. Carlier, B. Hwang, Simultaneous reduction of Co^{3+} and Mn^{4+} in P2-$Na_{2/3}Co_{2/3}Mn_{1/3}O_2$ as evidenced by X-ray absorption spectroscopy during electrochemical sodium intercalation, Chem. Mater. 26 (2014) 1219–1225.

[53] X. Xu, S. Ji, R. Gao, J. Liu, Facile synthesis of P2-type $Na_{0.4}Mn_{0.54}Co_{0.46}O_2$ as a high capacity cathode material for sodium-ion batteries, RSC Adv. 5 (2015) 51454–51460.

[54] N. Bucher, S. Hartung, I. Gocheva, Y.L. Cheah, M. Srinivasan, H.E. Hoster, Combustion-synthesized sodium manganese (cobalt) Oxides as cathodes for sodium ion batteries, J. Solid State Electrochem. 17 (2013) 1923–1929.

[55] J.M. Paulsen, J.R. Dahn, Studies of the layered manganese bronzes, $Na_{2/3}[Mn_{1-x}M_x]O_2$ with M = Co, Ni, Li, and $Li_{2/3}[Mn_{1-x}M_x]O_2$ prepared by ion-exchange, Solid State Ionics 126 (1999) 3–24.

[56] R. Wang, S. Wang, X. Peng, Y. Zhang, D. Jin, P.K. Chu, L. Zhang, Elusidating the intercalation pseudocapacitance mechanism of MoS2-carbon monolayer interoverlaped structure: toward high performance sodium ion based hybrid supercapacitor, ACS Appl. Mater. Interfaces 9 (2017) 32745–32755.